Version of Record: https://www.sciencedirect.com/science/article/pii/S0021979720310304
Manuscript_76674676910cf67a55a79e3c0a180e37

Microstructure-driven self-assembly and rheological properties of multi-responsive soft microgel suspensions

Eva Dieuzy[1,2,3] ‡, *Garbine Aguirre*[1,3] ‡, *Stéphane Auguste,*[3,4] *Kamel Chougrani,*[5] *Valérie Alard,*[5] *Laurent Billon,* [1,2,3] * *Christophe Derail* [1,2] *

[1]*Universite de Pau et Pays de l'Adour, E2S UPPA, CNRS, Institut des Sciences Analytiques & de PhysicoChimie pour l'Environnement & les Matériaux, UMR5254, 64000, PAU, France*

[2]*LERAM, LabCom UPPA/URGO, Hélioparc, 2 avenue Angot, 64053 Pau*

[3]*Bio-inspired Materials group: Functionalities & Self-assembly, E2S UPPA, Hélioparc, 2 avenue Angot, 64053, Pau.*

[4] *URGO RECHERCHE INNOVATION ET DEVELOPPEMENT ; 42 Rue de Longvic, 21300 Chenôve, France*

[5]*LVMH Recherche Parfums et Cosmétiques ; 185 Av. De Verdun, St Jean de Braye F-45804, France.*

Abstract

Hypotheses

The deformation and swelling ability of microgels is influenced by the crosslinking distribution. Varying microgels microstructure is expected to obtain suspensions with different flow behavior and thereby, different rheological properties.

Experiments

Different multi-responsive microgels were synthesized using two different crosslinkers and varying their amounts: N,N-methylene bis-acrylamide (MBA) and oligo(ethylene glycol) diacrylate (OEGDA). The rheological results were obtained by zero-shear viscosity and long-time creep measurements on concentrated microgel suspensions Microgel microstructure was analyzed by ^{1}H nuclear magnetic resonance transverse relaxation measurements.

Findings

At a constant crosslinking rate, we show that the viscosity of OEGDA-crosslinked microgels diverges at a higher concentration than MBA ones, suggesting a looser shell and less restricted dangling chains at the periphery for the later. By scaling with the effective volume fraction, the viscosity curves of the different microgel suspensions reduce into a single curve and closely follow hard sphere models up to $\phi_{eff} < 0.45$. The results from creep tests revealed a much higher yield stress for MBA-crosslinked microgels, strengthening the hypothesis of a looser shell for the later. Finally, transverse relaxation (T_2) NMR measurements demonstrated that, although all microgels exhibit a core-shell microstructure, MBA samples present a less crosslinked shell corroborating with the rheological results.

Keywords: microgels, stimuli-responsive, microstructure, rheology, yield stress

Introduction

Microgels are colloidal particles that are composed of cross-linked polymeric networks swollen in a good solvent.[1] Thanks to their high swelling ability, microgels are attractive for food, cosmetic and pharmaceutical applications, in which they are commonly used as texture modifiers[2–4] or bioactive delivery systems.[5,6] In contrast to hard sphere systems, microgels are deformable particles that present a hairy surface of swollen dangling chains. The soft structure strongly affects the flow behavior of suspensions, especially when particles enter in close contact. It is well-established that, above a critical volume fraction, hard particles form a dense network that exhibits solid-like properties, including elasticity and yield stress.[7] This critical volume fraction corresponds to the random close packing, noted RCP, ($\phi_{RCP} \approx 0.64$) for monodispersed hard spheres.[8] However, it is greatly influenced by the particle characteristics such as size, shape or polydispersity.[9–11] Microgels represent a much richer and more complex system than hard spheres due to their softness and to their structure. At high concentration, microgels may undergo deformation, interpenetration and deswelling which enable the suspension to be concentrated at higher volume fraction than the physical limit of RCP.[12–15] Crosslinking density of microgels, which directly impacts the deformation and deswelling capacity, represents an important lever to tune the rheological characteristics such as viscosity, modulus and yield stress.[16,17]

Furthermore, the possibility to synthesize stimuli-responsive microgels, such as thermo- and pH-sensitive ones, have brought considerable interest both in academia and industry. Poly(N-isopropylacrylamide)-based microgels are considered as model thermo-responsive systems and have been widely studied in view of their high encapsulation efficiency. The Lower Critical

Solution Temperature (LSCT) of PNiPAM chains at around 32°C induces a sharp volume transition of microgels at about the same temperature.[18] Such thermo-responsive behavior leads to interesting rheological features, such as the tunability of the effective volume fraction by the temperature for a constant particle concentration. More interestingly, at the swollen-to-collapse transition, the suspension evolves from a repulsive to an attractive system due to the change of solvent quality, resulting in the disappearance of steric forces for example.[19,20] While the influence of crosslinking density on the flow behavior of microgels has been extensively investigated, rheological studies on the impact of the microgel microstructure are scarce. Yet, one can expect that the microstructure of microgels in terms of crosslinking distribution probably affects as much the flow behavior since it also influences the swelling ability. Regarding the microstructure of the microgels, the general concept for microgels prepared by batch emulsion/precipitation polymerization is a core-shell model in which core and shell have different structures and crosslinking degrees.[21,22] The reason of this heterogeneous crosslinking density distribution is the faster reaction rate of crosslinkers than that of main monomers.[23] Up to now, the heterogeneous microgel structure has been studied using different techniques such as static light scattering,[24] small-angle neutron scattering (SANS),[14,25,26] and ^{1}H-nuclear magnetic resonance (^{1}H NMR) transverse relaxation measurements.[21,27,28]

Recently, Balaceanu and coworkers reported Flory temperature-induced volume transition theory for homopolymer microgels with bimodal heterogeneous morphology. [28-29] In the same way, Pikabea *et al.* generalized the theory for thermo- and pH-responsive nanogels with different bimodal heterogeneous morphologies.[30] In these works, the quantitative characterization of core-shell morphology such as the number of chains between two crosslinking points into the core and shell and the relative volume of the core, was possible thanks to some microscopic and

thermodynamic constraints imposed by ^{1}H-transverse relaxation NMR and Flory equation of state.

The novelty of this contribution comes from the study of the effect of different crosslinkers on the thermo- and pH-responsive microgels rheological behavior together with the understanding of their inner structure effect on their rheological properties. Although up to now, multi-responsive microgels based on PNIPAM are the most studied ones in terms of thermo-responsiveness, the use of poly(oligoethylene glycol) methacrylates (POEGMA) could be a better alternative thanks to their biocompatibility in the design of multi-responsive microgels.[32,33] In this sense, biocompatible oligo(ethylene glycol)-based microgels were synthesized by precipitation polymerization using as reference the procedure reported by Boularas *et al.*[22]. They suggested the different conversion rates of the crosslinkers should induce different complex microstructures, such as homogeneous and core-shell ones. During the solvent evaporation, the suspensions successively evolve from a fluid to a soft paste, and finally to a viscoelastic film thanks to the self-assembly of microgels.[6, 31] In a first step, the present study aimed at using rheology as a tool to get insight on the microgel microstructure and formulate hypotheses on the difference in fuzziness caused by the crosslinker type and rate. Indeed, the interactions between microgels during flow in a crowded state can reveal understanding of the microstructure of the particle itself. In a second step, the objective was to confirm these hypotheses using proton transverse relaxation NMR measurements. The understanding of the particle microstructure will be extremely helpful at a later stage to discuss about the mechanical properties of films formed on the self-assembly of microgels. The study of the film properties will be the central subject of a coming publication. In this work, the influence of the crosslinking density and crosslinking distribution was investigated by varying respectively the crosslinker rate (2 mol.% *versus* 8

mol.%) and the crosslinker type (OEGDA *versus* MBA). Although the impact of crosslinking density is well-described in the literature, the motivation to study a higher crosslinking rate was to validate the suitability of the rheological tests in revealing structural differences for a known microstructure. Zero-shear viscosity and creep tests were performed to investigate the flow and yielding behavior of these four microgel suspensions. Since the investigation of microstructure is the main objective, the study focused on measurements under the volume phase transition, that is to say when microgels are swollen and dominated by repulsive electro-steric forces. To confirm the macroscopic hypotheses based on the rheology study, the microgels microstructure was determined by proton transverse relaxation NMR measurements together with the application of Flory-Rehner theory to our microgels.

Materials & Methods

Materials. Di(ethylene glycol) methyl ether methacrylate (MEO_2MA, 95%), oligo(ethylene glycol) methyl ether methacrylate (OEGMA, terminated by 8 EG units with Mn=475 g·mol^(−1)), methacrylic acid (MAA), poly(ethylene glycol) diacrylate (OEGDA, Mn=250 g·mol^(−1)), N,N-methylenebisacrylamide (MBA) and potassium persulfate (KPS) were purchased from Sigma Aldrich and used as received. Deuterium oxide (D_2O), supplied by Eurisotop, was used for NMR characterization. Purified water from a Millipore Milli-Q system was used.

Microgel synthesis. The precipitation polymerization of microgels is carried out in a 2 L jacketed glass reactor by following the procedure previously described by Boularas *et al.*[35,36] Briefly, MEO_2MA (92.6 mmol), OEGMA (10.3 mmol) and varying amounts of crosslinker,

either OEGDA or MBA, are dissolved in 930 g of water. The crosslinker ratios are set at 2 mol.%, and 8 mol.% *versus* the total vinylic molecules, respectively corresponding to 2.12 mmol, and 9.42 mmol. The mixture is introduced in the 2 L reactor and stirring is set at 150 rpm. The reactor is purged with nitrogen for 45 min to remove oxygen at room temperature. MAA (5.41 mmol) is dissolved in 30 g of water and added to the reactor. The mixture is heated to 70°C. Finally, KPS (0.958 mmol) is dissolved in 40 g of water and injected into the reactor to start the reaction. The reaction is kept at 70°C during 6 hours. At the end of synthesis, microgels are purified by 3 centrifugation cycles (20,000 rpm, 20 min). The microgel suspensions are abbreviated by the molar ratio and the crosslinker type. The four systems studied are then called: 2-MBA, 2-OEGDA, 8-MBA and 8-OEGDA.

Methods. Hydrodynamic diameters (D_h) were measured by Dynamic Light Scattering (DLS) on a Zetasizer Nano (Malvern), at an angle of 173° and a laser wavelength of 633 nm. Microgel dispersions were diluted to a concentration of c = 1 $mg.mL^{-1}$. Temperature ramps were realized from 20°C to 60°C, with 3 measurements each 2.5°C. A stabilization time of 10 minutes was used between each set of measurements.

The relative viscosity of dilute suspensions was investigated with a homemade computer-controlled capillary viscosimeter developed by Rodriguez *et al.*[37] Five to six concentrations of dilute suspensions were measured for each samples.

The rheological measurements of concentrated suspensions were performed on a stress-controlled Bolhin Gemini (Malvern) using a concentric cylinder geometry (inner and outer diameters: 25mm and 27.5 mm). Measurements were carried out after equilibrating the samples at a constant temperature. Shear viscosity measurements were performed by applying a ramp up and down of shear rate. Shearing time was set at t=20s in order to reach steady state. Before each

test, a high rate steady shear (50 s^{-1}) was imposed to the suspension during 30s followed by a waiting time of 10min for the suspension to equilibrate at the set temperature. Long-time creep tests consisted of applying a constant stress (σ_c) during 600 s and recording the strain (γ), or equivalently the compliance $J(t) = \gamma/\sigma_c$.

The core volume fraction was calculated using the weight concentration c and the polymer density ρ (Eq.1). The polymer density was set at 1.2 $g.cm^{-3}$ considering the density of a linear PEG polymer.

$$\phi_{core} = \frac{c}{\rho} \quad (1)$$

The effective volume fraction was converted from the weight concentration by using a proportional factor determined with the dilute viscosity measurements. Curves and proportional factors for each system are presented in SI.

The microstructure of the microgels synthesized was analyzed by high-resolution transverse relaxation (T_2) NMR measurements using the protocol presented by other authors with some modifications.[29,31] For these measurements a 2 wt% of microgels dissolved in deuterated water were used. All NMR experiments were performed at 25 °C on a Bruker Avance 400 spectrometer equipped with a Bruker 5 mm BBFO. The proton chemical shifts were referenced to the HOD signal at 4.70 ppm. Transverse relaxation (T2) values were determined using the Carr−Purcell−Meiboom−Gill (CPMG) pulse sequence using 10 values of spin−echo time (τ), with a minimum of 2 ms and a maximum of 1500 ms. The delay between 180° pulses in the CPMG block was 1.5 ms, and the number of scans was set at 64 and D1 at 5 s. The temperature was controlled by a Bruker temperature controller, which kept the sample temperature stable at 25°C.

Results & discussions

Swelling ability of microgels. The hydrodynamic diameters of microgels were analyzed by Dynamic Light Scattering (DLS) in order to evaluate the impact of the crosslinking density and distribution on the swelling ability. Figure 1 (A) and (B) shows the hydrodynamic diameters of OEGDA- and MBA-crosslinked microgels in a dilute solution at pH 6 for temperature ranging from 20°C to 60°C. As can be observed, microgels synthesized present the conventional thermal behavior, being highly swollen below VPTT and shrunken above the critical temperature due to the increase in the hydrophobic interactions between non-polar groups.[22,23] The swelling ratios $\Phi_{20/60°C}$, *i.e.* ratio of hydrodynamic diameter at 20°C over hydrodynamic diameter at 60°C, are summarized in Table S1. The less crosslinked microgels exhibit the highest swelling ratio, such as $\Phi_{20/60°C} = 17.3$ for 2 mol.% OEGDA-crosslinked microgels whereas $\Phi_{20/60°C} = 6.3$ for 8 mol.% OEGDA-crosslinked ones. The Volume Phase Transition temperature (VPTT) is not significantly influenced by the crosslinking density, as it was previously described in several studies on microgels and macroscopic gels.[38] However, an increasing crosslinking density induces a much more gradual volume phase transition as also reported in other studies. [38–40] A more gradual transition was ascribed by Woodward *et al.* to a decreased in the enthalpic energy of conformational change for higher crosslinker amount. The crosslinking points delay the conformational change of the thermoresponsive chains resulting in a larger range of temperatures corresponding to the VPPT. A more progressive VPT has also been ascribed to a more heterogenous structure, as previously reported by Pikabea *et al.* and Wu and Zhou.[31,41] The increase in crosslinking content from 2 to 8 mol.% may enhance the heterogeneity of the microgel structure leading to a very progressive transition. OEGDA-crosslinked microgels exhibit a higher swelling ratio compared to MBA-crosslinked ones, regardless of the crosslinker

content. With 8 mol. % of crosslinker, OEGDA swelling ratio, $\Phi_{20/60°C}$, is around 6.3 compared to 3.1 for MBA one. As it was described by Imaz *et al.*[42], OEGDA crosslinker (M_n=250 g·mol^(−1)) is a much longer spacer than MBA, which offers a higher flexibility to the microgel network and enhances its swelling ability. Furthermore, the microgels are more hydrophilic with the addition of OEGDA than MBA which lead to higher swelling abilities. The volume phase transition of 2-MBA is slightly more gradual than 2-OEGDA. As previously discussed, the gradual volume phase transition is commonly attributed to the heterogeneity in crosslinker distribution into the microgel network. Thus, the slightly broader phase transition of 2-MBA sample could come from a more heterogeneous distribution of the crosslinker molecules within the microgel.

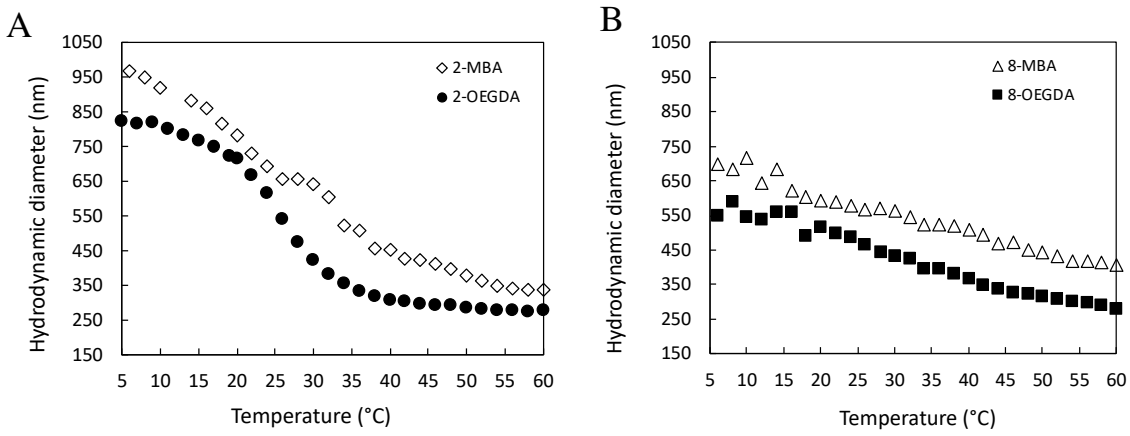

Figure 1. (A) Hydrodynamic diameters *versus* temperature of 2-OEGDA and 2-MBA microgels in buffer of pH 6. (B) Hydrodynamic diameters *versus* temperature of 8-OEGDA and 8-MBA microgels in buffer of pH 6

Rheological behavior of microgels. Figure 2 shows the viscosity as a function of shear rate of 2 mol.% MBA-crosslinked microgels for weight concentrations between 5 wt. % and 20 wt.%. The data for the other systems can be found in supporting information (Figures S1-S3). At low

concentration, the suspensions behave as Newtonian fluids *i.e.* viscosity does not vary with shear rate. At higher concentration, the suspensions exhibit the typical shear rate dependence of concentrated colloidal suspensions, namely shear thinning and a plateau at high and low shear rates. No difference in viscosity is observed between the ramp up and the ramp down, which is characteristic of repulsive systems. Indeed, the negative charges coming from methacrylic acid units and the swollen dangling chains of microgels give rise to electro-steric repulsive forces that prevent particle attraction. Since particles do not aggregate, the shear rate-driven microstructure remains the same during both ramps. Figure 3 shows the rapid drop in viscosity for temperature decreasing from 14°C to 36°C for a 16.9 wt% 2-OEGDA sample. Indeed, a temperature approaching ≈ 32°C induces the collapse of microgels and the decrease of the occupied volume for a same particle density. Microgels are more distant from each other leading to the decrease of viscosity. Once the temperature is above the VPTT, viscosity almost ceases to decrease since the hydrodynamic diameter of microgels reaches a plateau. Viscosity curves at low concentration were fitted with an equation developed by Cross[43] in order to extrapolate the zero-shear and high-shear viscosities, η_0 and η_∞ respectively:

$$\eta = \eta_\infty + \frac{\eta_0 - \eta_\infty}{1+(C\dot{\gamma})^m} \quad (2)$$

The fits according to Eq. (2) are represented by the dashed lines in Figure 2. The zero-shear viscosity is used to calculate the relative viscosity η_r expressed by $\eta_r = \eta_0 / \eta_s$, with η_s the solvent viscosity (taken at 0.001 Pa.s for Milli-Q water). To compare the systems, the relative viscosity is plotted as a function of the volume fraction in Figure 4 for the four suspensions. Since the swelling is not considered in the core volume fraction parameter, the viscosity diverges at a critical volume fraction ϕ^* much lower than the hard-sphere one, commonly taken at ≈ 0.58 for

repulsive glass.[44–46] The viscosity diverges at a higher volume fraction for increasing crosslinking densities of microgels. The influence of the crosslinker and the crosslinking density have been described in several studies.[16,47–49] In theta solvent, microgels are generally described as highly swollen and deformable spheres with a soft and fuzzy corona layer. As the concentration increases, those swollen microgels approach from one another resulting in a rapid increment of viscosity. It was repeatedly observed that for a same weight concentration, the viscosity of highly crosslinked microgels is much lower than the one of lightly crosslinked microgels. It was suggested that the lightly crosslinked microgels present longer-range interaction at larger separation distance due to their looser structure and softer steric layer thus, resulting in a higher viscosity. The increase in the degree of crosslinking reduces the swelling and hinders the microgel inter-particle bridging interaction.[48] Therefore, microgels crosslinked with the higher crosslinker rate (8 mol.%) resemble more to hard spheres and the viscosity diverges closer from the theoretical value of 0.58, such as observed in other work.[16] The type of crosslinker also strongly affects the rheological behavior of the suspensions. The zero-shear viscosity of 2-MBA sample diverges at a lower concentration than the 2-OEGDA one, and equivalently for 8 mol.% of crosslinker. This result is not in agreement with the DLS measurements that reveal a higher swelling ratio for OEGDA for both crosslinker rates (see Figure 1). At a theoretically equal crosslinker rate, one would expect MBA samples to diverge at higher volume fraction considering their lower swelling ability. This discrepancy could come from a different topology of the outer microgel shell induced by the different distribution of the crosslinking points within the particle being the shell of the microgels synthesized with MBA less crosslinked than that of OEGDA ones. This part will be further discussed by screening the microgel microstructure by NMR.

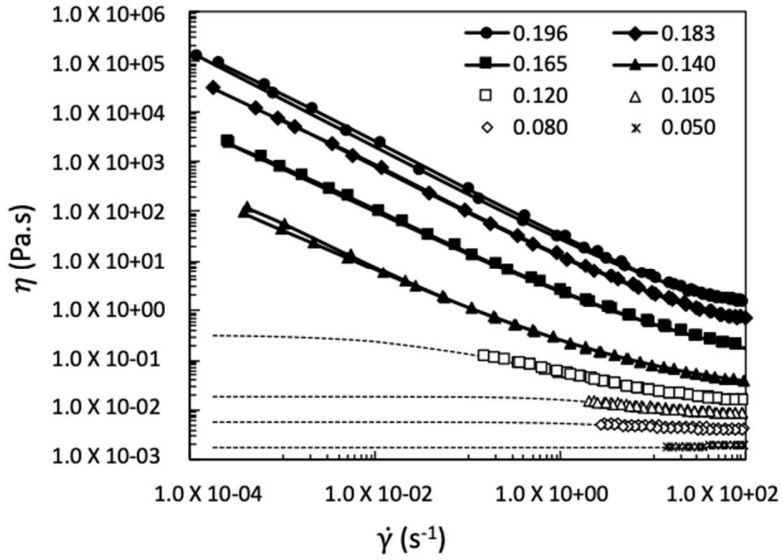

Figure 2: Viscosity as a function of shear rate for different weight concentrations of a 2-MBA sample. Ramp up and ramp down. The dashed lines represent the fits according to Cross Equation, Eq. (2).

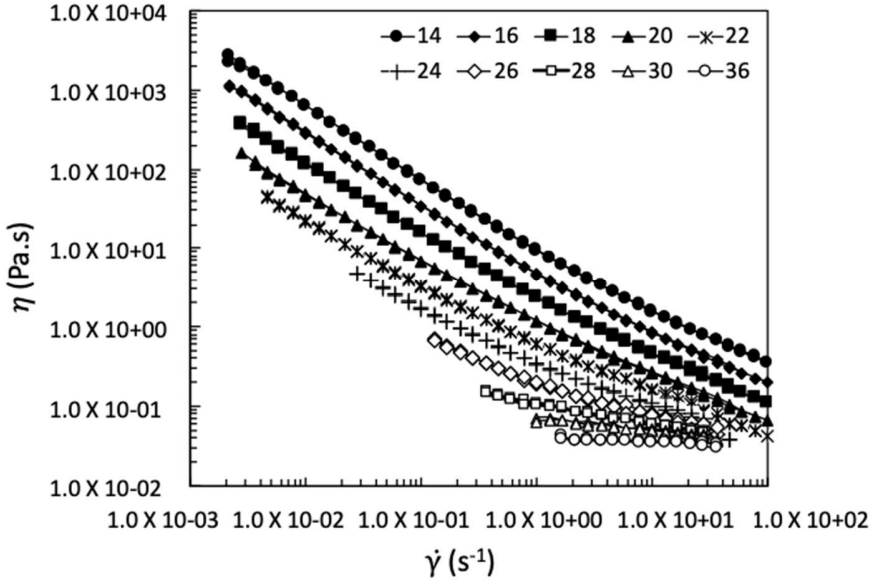

Figure 3: Viscosity as a function of shear rate for different temperatures of a 16.9 wt% 2-OEGDA sample. Ramp up and ramp down.

Microgels are compared to the rheological behavior of hard-sphere models by scaling the relative viscosity against the effective volume fraction ϕ_{eff} in Figure 4 (B). The effective volume fraction was determined through the measurements of the relative viscosity in dilute concentrations as commonly described.[47] The curves of the relative viscosity in dilute concentration are shown in Figure S6 for the four systems. One can outline that the limit of this method, based on measurements in dilute concentrations, is not to consider the eventual deswelling of microgels at high packing fraction. Indeed, microgels can undergo deswelling as the particle concentration increases due to steric compression of the overlapping chains between particles.[50] Thus, the effective volume fraction is surely less accurate at high packing fraction. The inherent difficulty to assess the value of the volume fraction regardless of the chosen method highlights the complexity of soft microgel systems compared to hard sphere, as reported by Lyon et al.[15]

As observed in Figure 4 (B), the relative viscosity curves of the four systems (2-MBA, 2-OEGDA, 8-MBA and 8-OEGDA) successfully reduce into a single master curve when plotted against ϕ_{eff}. The relative viscosity of concentrated hard sphere suspensions is commonly described by the Eq (3) named the Quemada equation:[51]

$$\eta_r = (1 - \frac{\phi}{\phi_{max}})^{-2} \quad (3)$$

Where ϕ_{max} is usually set at 0.64 for crystals and 0.58 for glass suspensions.

Or Eq. (4) named the Krieger-Dougherty equation:[52]

$$\eta_r = (1 - \frac{\phi}{\phi_{max}})^{-[\eta]\phi_{max}} \quad (4)$$

The Quemada equation with ϕ_{max}= 0.58 and ϕ_{max}= 0.64 is represented by the two black lines in Figure 4 (B). The different microgel suspensions are fairly well described by the hard sphere model until ≈ 0.45, regardless of the crosslinker type and density. It indicates that microgels can be seen as impermeable hydrodynamic particles in their non-draining behavior. At these crosslinking densities, the solvent is not flowing through microgels but moving along with its polymer chains. Data points from the most crosslinked suspensions, 8-OEGDA and 8-MBA, run particularly close to the Quemada hard sphere model. As one expects, the more the microgels are crosslinked, the more they resemble to hard spheres. The softer suspensions, 2-MBA and 2-OEGDA, diverge at a slightly lower effective volume fraction than the colloidal glass transition of hard spheres at 0.58. The samples are better described by a Krieger-Dougherty equation, represented by the dashed line in Figure 4 (B), for which ϕ_{max} is set at 0.48 and $[\eta]$ at 3. The early divergence of the relative viscosity of these samples is not in agreement with the divergence at high ϕ_{eff} usually described by the literature for soft systems.[12–14] Although the reason of the divergence at higher ϕ_{eff} is commonly attributed to the deformation of soft particles, some authors stated it could also be caused by high polydispersity.[47] The polydispersity indexes measured with DLS at 20°C, are found to be lower than 5% for the four samples, as seen in Table S2. Such low polydispersity is suitable for a fluid-crystal coexistence regime, since previous studies have demonstrated that polydispersity should be higher than ≈ 8% to prevents the formation of crystal regions.[9,10,53,54] Yet, the polydispersity indexes being very similar for the four systems, the early viscosity divergence seems to be driven by the microstructure of the softer microgels. One can suppose the numerous dangling chains of the microgel shell may hinder the particle motion by creating friction and interpenetration as soon as particles are

packed. The particle deformation occurs at higher concentrations, when the system is already dynamically arrested by friction and interpenetration.

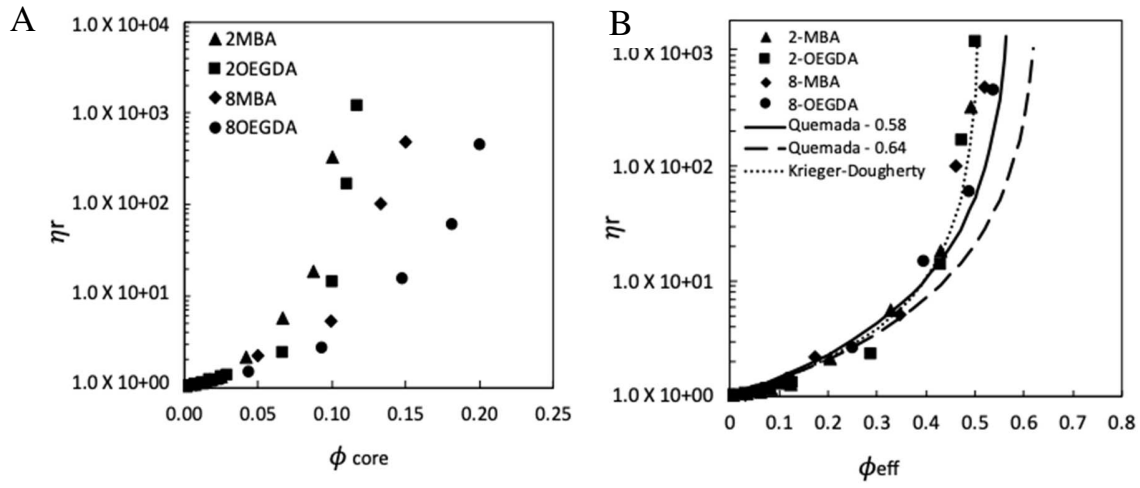

Figure 4: (A) Relative viscosity as a function of the core volume fraction for 2-MBA, 2-OEGDA, 8-MBA and 8-OEGDA samples (B) Relative viscosity as a function of effective volume fraction for 2-MBA, 2-OEGDA, 8-MBA and 8-OEGDA samples. The solid and dashed lines represent the hard sphere behavior according to Quemada equation with respectively ϕ_{max}= 0.58 and ϕ_{max}= 0.64. The dotted line corresponds to the Krieger-Dougherty equation where the parameters were set to obtain the best fit, accordingly ϕ_{max}= 0.48 and $[\eta]$=3.

Stress data from shear viscosity measurements are plotted against shear rate in Figure 5 (A) and (B) for respectively 2-MBA and 2-OEGDA sample. The data for 8-OEGDA and 8-MBA can be found in supporting information (S4 and S5). Above the critical volume fraction at which viscosity diverges, the suspensions exhibit elastic properties including a yield stress. The curves

above ϕ* are fitted by a Herschel-Bulckley model which is known to well described the rheological behavior of simple yield stress fluids as proposed in Eq. 5:

$$\sigma = \sigma_y + K_{HB}(\dot{\gamma})^n \quad (5)$$

with σ_y the yield stress, K_{HB} the consistency index and n the flow index. The difference induced by the crosslinker type is even more pronounced for volume fraction above ϕ*, once the particles are densely packed. As a comparison, for a similar concentration of ≈ 18 wt. %, the yield stress, extrapolated from the HB fit, of 2-MBA is about 50 times greater than 2-OEGDA one, respectively 5.72 Pa and 0.12 Pa.

However, rather than measuring shear viscosity, elastic properties of repulsive glasses are most commonly characterized with oscillatory shear or creep measurements which represent the proper method to determine a yield stress.[7,55–59] In previous works, Senff and Richtering[47] indicated that the yield stress was more relevant to reveal the chain topology at the microgel shell whereas the moduli in oscillatory shear are more dependent on the crosslinking degree within the microgels. Thus, long-time creep tests were performed in order to further investigate the hypothesis of a looser crosslinked shell in MBA samples.

A

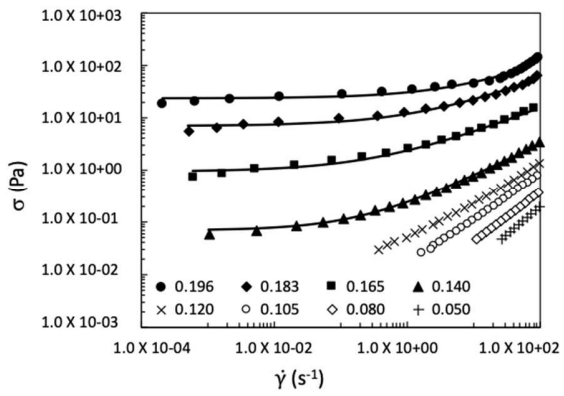

B

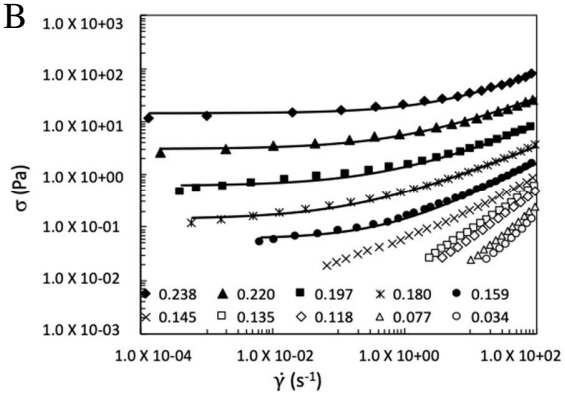

Figure 5: Stress as a function of shear rate for different weight concentrations of (A) 2-MBA suspension (B) 2-OEGDA suspension. The solid lines are fits according the Herschel-Bulckley equation.

The compliance *vs* time curves are represented in Figure 6 (A) and (B) for 2-OEGDA and 2-MBA samples at a concentration of 18 wt. %. Increasing transient stresses were applied until the suspensions exhibit complete flow. The oscillations at the start of a creep test, especially observed for 2-OEGDA sample, come from the instrument inertia coupled with the sample elasticity.[60] For stresses greater than the yield stress σ_y, the increase of strain is linear with time. The slope of 1 in the log-log plot expresses the fully developed flow of the suspensions. For stresses smaller than σ_y, the strain does not reach a plateau with long time, as it could be expected for an ideal solid. It increases in a sublinear manner without reaching a fully developed flow. For the sake of comparison, the last decades of the compliance curves are fitted by an empirical power-law: $J(t) \propto t^{\lambda}$, as described by Pham *et al.*[59], although no theoretical justification supports its use. The increase of the exponent value illustrates well the solid-to-liquid transition. The complete flow of the system is described by $\lambda = 1$, and the associated stress can be taken as the yield stress. As observed in the semi-log plot in Figure 6 (C), the yield stress of 2-MBA corresponds to 5.00 Pa, whereas the yield of 2-OEGDA occurs at 0.05 Pa. Both values corroborate well with the yield stresses extrapolated from shear viscosity data, respectively 5.72 Pa and 0.12 Pa. A much greater stress is required to break down the particle assembly of the 2-MBA sample, revealing a stronger network of microgels. As it is well known, at such a highly concentrated state, microgels deform and interpenetrate between each other. These results strengthen the idea that the shell of 2-MBA has a higher capacity to interpenetrate. Most likely, the shell is composed of longer and loosely crosslinked dangling chains that are more suitable for

entanglement. Yet, the samples undergo a similar yielding mechanism, although not occurring at the same value. Indeed, the evolution of λ with σ_c is sharp from 0 to 1, describing an abrupt transition from creep to flow for both 2-MBA and 2-OEGDA. This is characteristic of repulsive-dominated suspensions, where the sharp transition is physically interpreted by the sudden cage breaking.[61–63] Despite the friction due to chain entanglements, the electro-steric repulsive forces, generated by the negative charges and the swollen dangling chains, dominate the yielding mechanism. Further structural characterization was undertaken by ^{1}H NMR transverse relaxation measurements to validate our hypothesis and quantitatively investigate the microstructure induced by the crosslinkers.

A

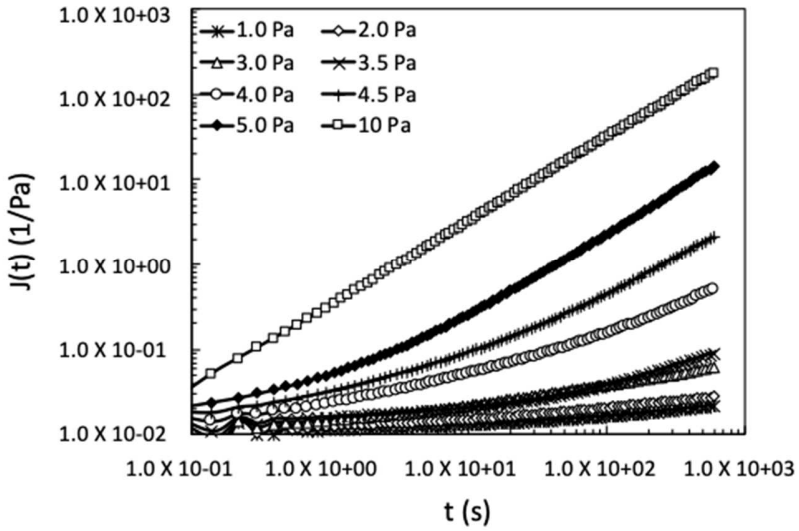

B

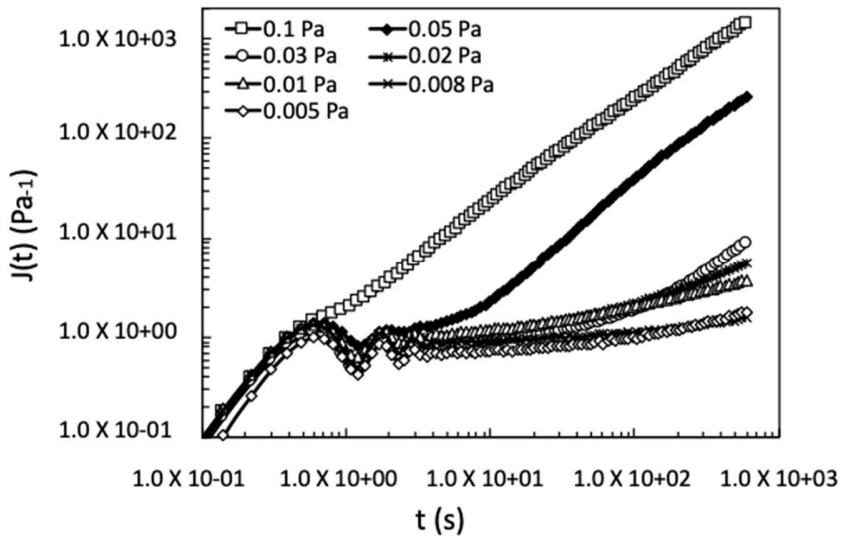

C

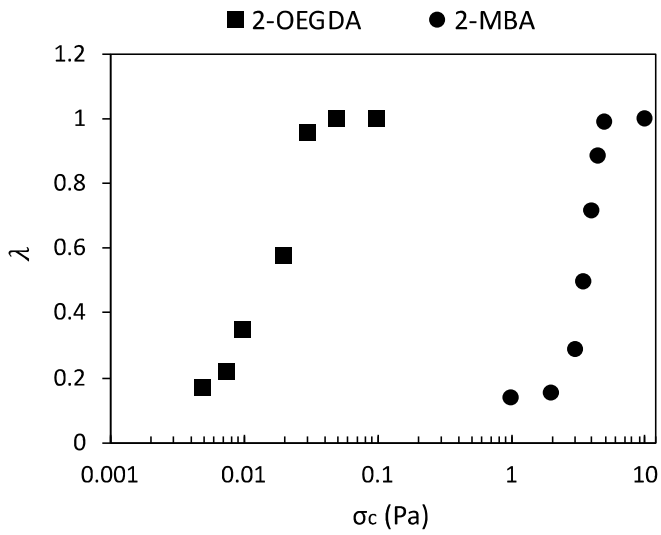

Figure 6: Compliance curves as a function of time for different constant stresses applied for (A) 2-MBA suspension (B) 2-OEGDA suspension. (C) Exponent λ from the power law $J(t) \propto t^{\lambda}$ *versus* the applied stresses for 2-MBA and 2-OEGDA samples

Microstructure of microgels. With the aim of linking the particle microstructure to macroscopic properties, ^{1}H-nuclear magnetic resonance (NMR) transverse relaxation

measurements were carried out. To investigate the heterogeneity in microstructure of the different microgel particles, the resonance peak that appears at 3.6 ppm of methylene protons of ($PMeO_2MA$-OEGMA) chains was used due to its high intensity (see Figure S1). Biexponential decay for the integral of methylene protons for the different microgels was assumed. Then, using the equations suggested by Balaceanu *et al.*,[29] short (T_{2S}) and long (T_{2L}) transverse relaxation times together with the relative amounts of methylene protons of ($PMeO_2MA$-OEGMA) chains in core (C_S) and shell (C_L) were obtained describing quantitatively the bimodal heterogeneity of the polymer network in microgel particles. In addition, the ratio of the crosslinking densities (CLD^{core}/CLD^{shell}) of the microgels was obtained from eq (6):

$$\frac{CLD^{core}}{CLD^{shell}} = \left(\frac{T_{2L}}{T_{2S}}\right)^{1/2} \quad (6)$$

The relative amounts of methylene protons of ($PMeO_2MA$-OEGMA) (C_S and C_L) and the ratios of crosslinking densities (CLD^{core}/CLD^{shell}) are reported in Table 1. As can be observed, regardless of the type and amount of crosslinker used, the C_S and C_L values are similar, in all the cases. This expected result can be understood considering the polymerization kinetics of MeO_2MA and OEGMA monomers. Boularas *et al.*[22] reported that the consumption rates of both monomers were not affected by the crosslinker type leading to a similar distribution of $PMeO_2MA$-OEGMA chains into the microgel particles. Similar results were reported by other authors in the case of poly(vinylcaprolactam) (PVCL)[21] and poly(2-diethylaminoethyl) methacrylate (PDEAEMA)[27] -based nanogels.

Table 1. Relative weight coefficient of ($PMeO_2MA$-OEGMA) chains in the core (C_S) and shell (C_L) and crosslinking density ratios (CLD^{core}/CLD^{shell}) of microgels cross-linked with OEGDA and MBA.

Crosslinker	C_S	C_L	CLD^{core}/CLD^{shell}
OEGDA (2 mol %)	0.49	0.57	5.3
MBA (2 mol %)	0.51	0.57	3.5
OEGDA (8 mol %)	0.46	0.60	3.8
MBA (8 mol %)	0.51	0.51	3.4

Regarding crosslinking density ratios, a core-shell microstructure is obtained in all the cases. Moreover, an effect of the crosslinker type and amount on the crosslinking density ratio and thus on the heterogeneity of the morphology is observed. In this sense, the lowest crosslinking density ratio was obtained by using MBA as crosslinker. The reason of that could be the difference between the reactivities of both crosslinkers (MBA and OEGMA) when they copolymerize with methacrylates, in this case, MeO_2MA and OEGMA. To confirm this hypothesis, the reactivity ratios of MBA and OEGDA with respect of OEGMA were determined by ^1H NMR following the method described by Mahdavian *et al.*[64] It was determined that MBA (r_{OEGMA} = 1.84 and r_{MBA} = 0.98) is less reactive than OEGMA (r_{OEGMA} = 1.19 and r_{OEGDA} = 1.12) when copolymerized with OEGMA leading to a more homogeneous core-shell structure. In addition, increasing the amount of MBA no effect on crosslinking density is observed. This means that the

ratio between core and shell, in terms of mobility, is not change with the increase in the amount of MBA. The same behavior was obtained by Balaceanu *et al.*[29] for PVCL-based microgels prepared with different amounts of MBA as a crosslinker. In the case of OEGDA crosslinker, increasing its concentration, the crosslinking ratio decreases from 5.3 to 3.8 being more similar to the values obtained in the case of using MBA as crosslinker.

Moreover, the study of the microgels microstructure could be related with the results obtained analyzing the rheological properties of microgel suspensions. As mentioned before, microgels particles cross-linked with MBA present better interpenetration with a strong capacity to assemble into structured network than OEGDA cross-linked microgel particles in all the crosslinker concentration range studied. This could be due to the crosslinking density difference observed in both types of microgels. In the interpenetration process, the shell of the particles is more involved than the core. In the case of microgels cross-linked with MBA the crosslinking density of the shell could be lower than that of OEGDA cross-linked ones leading to an easier interpenetration of the microgel particles. With the aim of corroborating this hypothesis, the Flory-Rehner theory was applied to the microgel synthesized.

In this regard, Balaceanu *et al*. reported an extended Flory-Rehner theory for thermoresponsive microgels based on a bimodal crosslinking density model.[29,30] Recently, Pikabea *et al*. applied the extended Flory-Rehner theory to analyze the inner structure of thermo- and pH-responsive nanogels.[31] Those authors reported that number of chains between two crosslinking points, *i.e*. subchains, was proportional to the relative weight coefficients of polymeric chains (C_L and C_S) and the relaxation times (T_{2S} and T_{2L}) measured by T_2 NMR experiments as described by Eq. (7):

$$\frac{N^{core}}{N^{shell}} = \frac{C_S}{C_L}\left(\frac{T_{2L}}{T_{2S}}\right)^{1/2} \quad (7)$$

Moreover, the number of subchains in the microgel particles can be estimated considering that each crosslinker molecule connects two subchains with the Eq. (8):

$$N = 2N_A v_0 c \quad (8)$$

where N_A is the Avogadro's constant, v_0 is the volume of each microgel particle and c is the molar concentration of crosslinker. Using the data obtained from above formulas, it is possible to calculate the proportionality parameter (ρ) between the radius of the core and the hydrodynamic radius of the microgel particles from the Eq.(9):

$$N = \frac{1}{2}\left(\frac{N^{core}}{\rho^3} + \frac{N^{shell}}{1-\rho^3}\right) \quad (9)$$

Table 2 shows the number of subchains in the core (N^{core}), number of subchains in the shell (N^{shell}) and the ratio between the radius of the core and the hydrodynamic radius of the microgel particles (ρ). It is important to point out that the parameter ρ is assumed to be temperature and pH independent.[29,31] As can be observed, in the case of microgels synthesized using MBA as crosslinker, the number of subchains in the shell is lower being this difference more important in the case of microgel synthesized with 8 mol% of crosslinker. Thus, although for both microgels the shell of the particles is less crosslinked allowing the interpenetration of the particles, in the case of the ones cross-linked with MBA the crosslinking density of the shell is even lower than that of OEGDA ones leading to a stronger capacity to assemble among them corroborating above hypothesis. These data do not agree with the hypothesis reported by Boularas *et al.*[21] suggesting a highly crosslinked shell and slightly crosslinked core in the case of microgels crosslinked with

MBA. They observed an impact of the crosslinker type on kinetic data by NMR during the analysis of non-purified microgel dispersions maybe because the impurities present in the dispersion could influence the results obtained. By contrast, in this work, purified microgel dispersions have been used during the determination of microgels microstructure and therefore, any external effect has been avoided. In summary, these results confirm that the different distribution of crosslinking points affects the rheological properties of microgel suspensions such as MBA samples exhibit a higher yield stress than OEGDA samples.

Table 2. Number of subchains in the core (N^{core}) and in the shell (N^{shell}) and the parameter ρ as a function of crosslinker type and amount (derived from Eq. (9)).

Crosslinker	$\mathbf{N^{core}}$	$\mathbf{N^{shell}}$	ρ
OEGDA (2 mol %)	13760	2870	0.87
MBA (2 mol %)	8480	2750	0.85
OEGDA (8 mol %)	1591200	600440	0.86
MBA (8 mol %)	456640	134300	0.86

In addition, similar values of the parameter ρ are obtained despite of the cross-linked type and amount used. The value of $\rho \approx 0.86$ means that the relative volume of the core is 66% of the total volume of the microgel particles. This value is much lower than that observed by Pikabea *et al*. for PDEAEMA-based nanogel particles (82%).[31] This larger shell could be one of the reasons of

the trigger-free spontaneous film formation properties presented by the microgels synthesized. These films present colored properties[1] and unusually high encapsulation values for different active molecules[2] being suitable for cosmetic and healthcare or medicine applications.

Conclusions

On the basis of the previously reported techniques for the microgels microstructure study [23-27], this work has demonstrated that differences in crosslinking density can be studied by coupling rheological tests and ^{1}H NMR transverse relaxation measurements.

The zero-shear viscosity and long-time creep tests on concentrated microgel suspensions have proved to be suitable techniques to reveal the differences in microstructure. Indeed, at higher crosslinking density, microgels resemble more to hard spheres and consequently, the relative viscosity diverges at a higher core volume fraction[15]. For both crosslinking rates, the viscosity of OEGDA samples diverges at a higher concentration than MBA ones, suggesting a looser crosslinked shell for MBA-crosslinked microgels. Creep tests revealed a higher yield stress for MBA samples than OEGDA ones for a same concentration, respectively 5 Pa and 0.05 Pa. These results strengthen the hypothesis of a looser crosslinked shell for MBA microstructure, which enables more interpenetration between particles, and thus leads to a stronger network. Yet, the transition from solid-to-liquid was sharp for both crosslinkers, indicating the microstructure did not affect the yielding mechanism[57-59]. In view of the small yield stress values, it can be noted that the suspensions, at this concentration, have very weak solid properties since an order of few Pascals is enough to trigger the solid-to-liquid transition. In this work, it was also demonstrated that the effective volume fraction is an appropriate scaling factor to compare microgels to the

hard sphere behavior. Indeed, the viscosity curves successfully reduce into a single curve and closely follow hard sphere models such as the Quemada relationship[47] up to $\phi_{eff} < 0.45$. The viscosities of softer suspensions do not diverge at higher ϕ_{eff} than the colloidal glass transition value, which is usually the case for soft systems[12-14]. One can suppose the numerous dangling chains of the microgel shell may hinder the particle motion by creating friction and interpenetration as soon as particles are densely packed. In this case, the particle deformation occurs when the system is already frozen, at higher concentrations. Finally, transverse relaxation (T_2) NMR measurements demonstrated that microgels exhibit a core-shell microstructure for both crosslinker types and both crosslinking densities, similar to what was observed for PVCL microgels crosslinked with different amounts of MBA[28]. Yet, MBA samples present a lower number of subchains in the shell, attesting of a less crosslinked shell. This result validates the hypotheses made in view of the rheological results.

In summary, the effect of different crosslinking architectures on particles assembly in suspension has been determined being the next step the study of its effect on self-assembled microgels film mechanical properties. Indeed, we already demonstrated during the solvent evaporation that the suspensions evolve from a fluid to a cohesive film thanks to the self-assembly of microgels[31] without characterization of the viscoelastic properties of the films towards the skin properties.

Associated comments

Swelling ratios and polydispersity indexes of microgels synthesized, viscosities and stresses of different microgels, relative viscosities of different microgels, proton spectrum of microgels cross-linked with OEGDA.

Author information

Corresponding Author

*E-mail: laurent.billon@univ-pau.fr; Tel: +33 559407609

*E-mail: christophe.derail@univ-pau.fr; Tel: +33 559407706

Author Contributions

The manuscript was written through contributions of all authors. All authors have given approval to the final version of the manuscript. ‡These authors contributed equally.

Acknowledge

E. Dieuzy is grateful to URGO RID, LVMH and the Région Nouvelle Aquitaine, convention 2016-1R10204-00007186 – THESE for her PhD financial support. Dr. G. Aguirre acknowledges NABITEX-SUDOE project for the financial support. This work benefits from the financial support of the French National Research Agency, convention Labcom ANR-14- LAB3-0003-01. The authors thank Dr. Abdel Khoukh for NMR measurements and discussion.

References

(1) Pelton, R. Temperature-Sensitive Aqueous Microgels. *Adv Colloid Interface Sci* **2000**, *85* (1), 1–33.

(2) Dickinson, E. Microgels — An Alternative Colloidal Ingredient for Stabilization of Food Emulsions. *Trends in Food Science & Technology* **2015**, *43* (2), 178–188.

(3) Ellis, A.; Jacquier, J. C. Manufacture of Food Grade κ-Carrageenan Microspheres. *Journal of Food Engineering* **2009**, *94* (3), 316–320.

(4) Norton, I. T. *Practical Food Rheology: An Interpretive Approach*; Wiley-Blackwell: Oxford, 2011.

(5) Malmsten, M. Microgels in Drug Delivery. *Microgel Suspensions* **2018**.

(6) Aguirre, G.; Khoukh, A.; Taboada, P.; Chougrani, K.; Alard, V.; Billon, L. Smart Self-Assembled Microgel Films as Encapsulating Carriers for UV-Absorbing Molecules. *Polymer*

Chemistry **2018**, *9* (10), 1155–1159.

(7) Petekidis, G.; Vlassopoulos, D.; Pusey, P. N. Yielding and Flow of Colloidal Glasses. *Faraday Discuss.* **2003**, *123* (0), 287–302.

(8) Buscall, R.; D'Haene, P.; Mewis, J. Maximum Density for Flow of Dispersions of Near Monodisperse Spherical Particles. *Langmuir* **1994**, *10* (5), 1439–1441.

(9) Auer, S.; Frenkel, D. Suppression of Crystal Nucleation in Polydisperse Colloids Due to Increase of the Surface Free Energy. *Nature* **2001**, *413* (6857), 711–713.

(10) Pusey, P. N.; Zaccarelli, E.; Valeriani, C.; Sanz, E.; Poon, W. C. K.; Cates, M. E. Hard Spheres: Crystallization and Glass Formation. *Philosophical Transactions of the Royal Society A: Mathematical, Physical and Engineering Sciences* **2009**, *367* (1909), 4993.

(11) Moriguchi, I.; Kawasaki, K.; Kawakatsu, T. The Effects of Size Polydispersity in Nearly Hard Sphere Colloids. *J. Phys. II France* **1993**, *3* (8), 1179–1184.

(12) Bodnár, I.; Silva, A. S.; Deitcher, R. W.; Weisman, N. E.; Kim, Y. H.; Wagner, N. J. Structure and Rheology of Hyperbranched and Dendritic Polymers. I. Modification and Characterization of Poly(Propyleneimine) Dendrimers with Acetyl Groups. *Journal of Polymer Science Part B: Polymer Physics* **2000**, *38* (6), 857–873.

(13) Vlassopoulos, D.; Fytas, G.; Pispas, S.; Hadjichristidis, N. Spherical Polymeric Brushes Viewed as Soft Colloidal Particles: Zero-Shear Viscosity. *Physica B: Condensed Matter* **2001**, *296* (1), 184–189.

(14) Stieger, M.; Pedersen, J. S.; Lindner, P.; Richtering, W. Are Thermoresponsive Microgels Model Systems for Concentrated Colloidal Suspensions? A Rheology and Small-Angle Neutron Scattering Study. *Langmuir* **2004**, *20* (17), 7283–7292.

(15) Lyon, L. A.; Fernandez-Nieves, A. The Polymer/Colloid Duality of Microgel Suspensions. *Annu. Rev. Phys. Chem.* **2012**, *63* (1), 25–43.

(16) Wolfe, M. S.; Scopazzi, C. Rheology of Swellable Microgel Dispersions: Influence of Crosslink Density. *Journal of Colloid and Interface Science* **1989**, *133* (1), 265–277.

(17) Vlassopoulos, D.; Cloitre, M. Tunable Rheology of Dense Soft Deformable Colloids. *Current Opinion in Colloid & Interface Science* **2014**, *19* (6), 561–574.

(18) Pelton, R. H.; Chibante, P. Preparation of Aqueous Latices with N-Isopropylacrylamide. *Colloids and Surfaces* **1986**, *20* (3), 247–256.

(19) Zhou, Z.; Jia, D.; Hollingsworth, J. V.; Cheng, H.; Han, C. C. From Repulsive to Attractive Glass: A Rheological Investigation. *J. Chem. Phys.* **2015**, *143* (23), 234901.

(20) Minami, S.; Watanabe, T.; Suzuki, D.; Urayama, K. Rheological Properties of Suspensions of Thermo-Responsive Poly(*N*-Isopropylacrylamide) Microgels Undergoing Volume Phase Transition. *Polymer Journal* **2016**, *48* (11), 1079–1086.

(21) Aguirre, G.; Ramos, J.; Forcada, J. Synthesis of New Enzymatically Degradable Thermo-Responsive Nanogels. *Soft Matter* **2012**, *9* (1), 261–270.

(22) Boularas, M.; Deniau-Lejeune, E.; Alard, V.; Tranchant, J.-F.; Billon, L.; Save, M. Dual Stimuli-Responsive Oligo(Ethylene Glycol)-Based Microgels: Insight into the Role of Internal Structure in Volume Phase Transitions and Loading of Magnetic Nanoparticles to Design Stable Thermoresponsive Hybrid Microgels. *Polymer Chemistry* **2016**, *7* (2), 350–363.

(23) Ramos, J.; Forcada, J.; Hidalgo-Alvarez, R. Cationic Polymer Nanoparticles and Nanogels: From Synthesis to Biotechnological Applications. *Chem. Rev.* **2014**, *114* (1), 367–428.

(24) Clara-Rahola, J.; Fernandez-Nieves, A.; Sierra-Martin, B.; South, A. B.; Lyon, L. A.; Kohlbrecher, J.; Fernandez Barbero, A. Structural Properties of Thermoresponsive Poly(N-Isopropylacrylamide)-Poly(Ethyleneglycol) Microgels. *J. Chem. Phys.* **2012**, *136* (21), 214903.

(25) Aguirre, G.; Deniau, E.; Brûlet, A.; Chougrani, K.; Alard, V.; Billon, L. Versatile Oligo(Ethylene Glycol)-Based Biocompatible Microgels for Loading/Release of Active Bio(Macro)Molecules. *Colloids and surfaces* **2019**.

(26) Saunders, B. R. On the Structure of Poly(N-Isopropylacrylamide) Microgel Particles. *Langmuir* **2004**, *20* (10), 3925–3932.

(27) Pikabea, A.; Ramos, J.; Forcada, J. Production of Cationic Nanogels with Potential Use in Controlled Drug Delivery. *Particle & Particle Systems Characterization* **2014**, *31* (1), 101–109.

(28) Schachschal, S.; Balaceanu, A.; Melian, C.; Demco, D. E.; Eckert, T.; Richtering, W.; Pich, A. Polyampholyte Microgels with Anionic Core and Cationic Shell. *Macromolecules* **2010**, *43* (9), 4331–4339.

(29) Balaceanu, A.; Demco, D. E.; Möller, M.; Pich, A. Microgel Heterogeneous Morphology Reflected in Temperature-Induced Volume Transition and 1H High-Resolution Transverse Relaxation NMR. The Case of Poly(N-Vinylcaprolactam) Microgel. *Macromolecules* **2011**, *44* (7), 2161–2169.

(30) Balaceanu, A.; Demco, D. E.; Möller, M.; Pich, A. Heterogeneous Morphology of Random Copolymer Microgels as Reflected in Temperature-Induced Volume Transition and 1H High-Resolution Transverse Relaxation NMR. *Macromolecular Chemistry and Physics* **2011**, *212* (22), 2467–2477.

(31) Pikabea, A.; Aguirre, G.; Miranda, J. I.; Ramos, J.; Forcada, J. Understanding of Nanogels Swelling Behavior through a Deep Insight into Their Morphology. *Journal of Polymer Science Part A: Polymer Chemistry* **2015**, *53* (17), 2017–2025.

(32) Cai, T.; Marquez, M.; Hu, Z. Monodisperse Thermoresponsive Microgels of Poly(Ethylene Glycol) Analogue-Based Biopolymers. *Langmuir* **2007**, *23* (17), 8663–8666.

(33) Chi, C.; Cai, T.; Hu, Z. Oligo(Ethylene Glycol)-Based Thermoresponsive Core−Shell Microgels. *Langmuir* **2009**, *25* (6), 3814–3819.

(34) Boularas, M.; Radji, S.; Gombart, E.; Tranchant, J.-F.; Alard, V.; Billon, L. Functional Film by Trigger-Free Self-Assembly of Adhesive Soft Microgels at Skin Temperature. *Materials & Design* **2018**, *147*, 19–27.

(35) Boularas, M. Synthèse de Microgels Biocompatibles, Hybrides et Stimulables Pour Des Applications Cosmétiques. PhD dissertation, Pau, 2015.

(36) Aguirre, G.; Khoukh, A.; Chougrani, K.; Alard, V.; Billon, L. Dual-Responsive Biocompatible Microgels as High Loaded Cargo: Understanding of Encapsulation/Release Driving Forces by NMR NOESY. *Polymer Chemistry* **2018**, *9* (6), 757–768.

(37) Rodriguez, L.; Mejia, A.; Reynaud, S.; Lespes, G.; Favero, C.; Antignard, S.; Giovannetti, B.; Gaillard, N.; Dupuis, G.; Loriau, M.; Jouenne, S.; Grassl, B. Monitoring Thermal and Mechanical Stability of Enhanced Oil Recovery (EOR) Acrylamide Based Polymers (PAM) Through Intrinsic Viscosity (IV) Determination Using a New Capillary Rheology Technique; Society of Petroleum Engineers, 2016.

(38) Inomata, H.; Wada, N.; Yagi, Y.; Goto, S.; Saito, S. Swelling Behaviours of N-Alkylacrylamide Gels in Water: Effects of Copolymerization and Crosslinking Density. *Polymer* **1995**, *36* (4), 875–877.

(39) Woodward, N. C.; Chowdhry, B. Z.; Snowden, M. J.; Leharne, S. A.; Griffiths, P. C.; Winnington, A. L. Calorimetric Investigation of the Influence of Cross-Linker Concentration on the Volume Phase Transition of Poly(*N* -Isopropylacrylamide) Colloidal Microgels. *Langmuir* **2003**, *19* (8), 3202–3211.

(40) Varga, I.; Gilányi, T.; Mészáros, R.; Filipcsei, G.; Zrínyi, M. Effect of Cross-Link Density on the Internal Structure of Poly(N-Isopropylacrylamide) Microgels. *J. Phys. Chem. B* **2001**, *105* (38), 9071–9076.

(41) Wu, C.; Zhou, S. Volume Phase Transition of Swollen Gels: Discontinuous or Continuous? *Macromolecules* **1997**, *30* (3), 574–576.

(42) Imaz, A.; Forcada, J. N-Vinylcaprolactam-Based Microgels: Effect of the Concentration and Type of Cross-Linker. *Journal of Polymer Science Part A: Polymer Chemistry* **2008**, *46* (8), 2766–2775.

(43) Cross, M. M. Rheology of Non-Newtonian Fluids: A New Flow Equation for Pseudoplastic Systems. *Journal of Colloid Science* **1965**, *20* (5), 417–437.

(44) Meeker, S. P.; Poon, W. C. K.; Pusey, P. N. Concentration Dependence of the Low-Shear Viscosity of Suspensions of Hard-Sphere Colloids. *Physical Review E* **1997**, *55*, 5718–5722.

(45) Phan, S.-E.; Russel, W. B.; Cheng, Z.; Zhu, J.; Chaikin, P. M.; Dunsmuir, J. H.; Ottewill, R. H. Phase Transition, Equation of State, and Limiting Shear Viscosities of Hard Sphere Dispersions. *Phys. Rev. E* **1996**, *54* (6), 6633–6645.

(46) Hunter, G. L.; Weeks, E. R. The Physics of the Colloidal Glass Transition. *Rep. Prog. Phys.* **2012**, *75* (6), 066501.

(47) Senff, H.; Richtering, W. Influence of Cross-Link Density on Rheological Properties of Temperature-Sensitive Microgel Suspensions. *Colloid and Polymer Science* **2000**, *278* (9), 830–840.

(48) Li, D.; Hsu, R.; Figura, B.; Jacobs, R.; Li, S.; Horvath, S.; Clifford, T.; Chari, K. Rheology and Structure of Surface Crosslinked Surfactant-Activated Microgels. *Soft Matter* **2016**, *12* (34), 7150–7158.

(49) Conley, G. M.; Zhang, C.; Aebischer, P.; Harden, J. L.; Scheffold, F. Relationship between Rheology and Structure of Interpenetrating, Deforming and Compressing Microgels. *Nat Commun* **2019**, *10* (1), 2436.

(50) Romeo, G.; Imperiali, L.; Kim, J.-W.; Fernández-Nieves, A.; Weitz, D. A. Origin of De-Swelling and Dynamics of Dense Ionic Microgel Suspensions. *The Journal of Chemical Physics* **2012**, *136* (12), 124905.

(51) Quemada, D. Rheology of Concentrated Disperse Systems and Minimum Energy Dissipation Principle. *Rheol Acta* **1977**, *16* (1), 82–94.

(52) Krieger, I. M.; Dougherty, T. J. A Mechanism for Non-Newtonian Flow in Suspensions of Rigid Spheres. *Transactions of the Society of Rheology* **1959**, *3* (1), 137–152.

(53) Williams, S. R.; Snook, I. K.; van Megen, W. Molecular Dynamics Study of the Stability of the Hard Sphere Glass. *Phys Rev E Stat Nonlin Soft Matter Phys* **2001**, *64* (2 Pt 1), 021506.

(54) Zaccarelli, E.; Valeriani, C.; Sanz, E.; Poon, W. C. K.; Cates, M. E.; Pusey, P. N. Crystallization of Hard-Sphere Glasses. *Phys. Rev. Lett.* **2009**, *103* (13), 135704.

(55) Mason, null; Weitz, null. Linear Viscoelasticity of Colloidal Hard Sphere Suspensions near the Glass Transition. *Phys. Rev. Lett.* **1995**, *75* (14), 2770–2773.

(56) Derec, C.; Ducouret, G.; Ajdari, A.; Lequeux, F. Aging and Nonlinear Rheology in Suspensions of Polyethylene Oxide-Protected Silica Particles. *Phys Rev E Stat Nonlin Soft Matter Phys* **2003**, *67* (6 Pt 1), 061403.

(57) Petekidis, G.; Moussaïd, A.; Pusey, P. N. Rearrangements in Hard-Sphere Glasses under Oscillatory Shear Strain. *Phys Rev E Stat Nonlin Soft Matter Phys* **2002**, *66* (5 Pt 1), 051402.

(58) Petekidis, G.; Vlassopoulos, D.; Pusey, P. N. Yielding and Flow of Sheared Colloidal Glasses. *J. Phys.: Condens. Matter* **2004**, *16* (38), S3955–S3963.

(59) Pham, K. N.; Petekidis, G.; Vlassopoulos, D.; Egelhaaf, S. U.; Poon, W. C. K.; Pusey, P. N. Yielding Behavior of Repulsion- and Attraction-Dominated Colloidal Glasses. *Journal of Rheology* **2008**, *52* (2), 649–676.

(60) Craciun, L.; Carreau, P. J.; Heuzey, M.-C.; van de Ven, T. G. M.; Moan, M. Rheological Properties of Concentrated Latex Suspensions of Poly(Styrene-Butadiene). *Rheol Acta* **2003**, *42* (5), 410–420.

(61) Bengtzelius, U.; Gotze, W.; Sjolander, A. Dynamics of Supercooled Liquids and the

Glass Transition. *J. Phys. C: Solid State Phys.* **1984**, *17* (33), 5915–5934.

(62) Leutheusser, E. Dynamical Model of the Liquid-Glass Transition. *Phys. Rev. A* **1984**, *29* (5), 2765–2773.

(63) van Megen, W.; Underwood, S. M. Glass Transition in Colloidal Hard Spheres: Measurement and Mode-Coupling-Theory Analysis of the Coherent Intermediate Scattering Function. *Phys. Rev. E* **1994**, *49* (5), 4206–4220.

(64) Mahdavian, A. R.; Abdollahi, M.; Mokhtabad, L.; Bijanzadeh, H. R.; Ziaee, F. Kinetic Study of Radical Polymerization. IV. Determination of Reactivity Ratio in Copolymerization of Styrene and Itaconic Acid by 1H-NMR. *Journal of Applied Polymer Science* **2006**, *101* (3), 2062–2069.

Simulation and experimental study of enzyme and reactant mixing in capillary electrophoresis based on-line methods

Marta Pelcová [a,b], Roman Řemínek [a,b], Friederike A. Sandbaumhüter [a], Richard A. Mosher [c], Zdeněk Glatz [b], Wolfgang Thormann [a,*]

[a] Clinical Pharmacology Laboratory, Institute for Infectious Diseases, University of Bern, Bern, Switzerland
[b] Department of Biochemistry, Faculty of Science, Masaryk University, Brno, Czech Republic
[c] RAM Software Solutions, Tucson, AZ, USA.

*) Correspondence:

Prof. Dr. Wolfgang Thormann

Clinical Pharmacology Laboratory, Institute for Infectious Diseases, University of Bern, Murtenstrasse 35, 3008 Bern, Switzerland

E-mail: wolfgang.thormann@ifik.unibe.ch, Tel: +41-31-632-32-88, Fax: +41-31-632-4997

Abstract

The establishment of an efficient reaction mixture represents a crucial part of capillary electrophoresis based on-line enzymatic assays. For ketamine N-demethylation to norketamine mediated by the cytochrome P450 3A4 enzyme, mixing of enzyme and reactants in the incubation buffer at physiological pH was studied by computer simulation. A dynamic electrophoretic simulator that encompasses Taylor-Aris diffusivity which accounts for dispersion due to the parabolic flow profile associated with pressure driven flow was utilized. The simulator in the diffusion mode was used to predict transverse diffusional reactant mixing occurring during hydrodynamic plug injection of configurations featuring four and seven plugs. The same simulator in the electrophoretic mode was applied to study electrophoretic reactant mixing caused by voltage application in absence of buffer flow. Resulting conclusions were experimentally verified with enantioselective analysis of norketamine in a background electrolyte at low pH. Furthermore, simulations visualize buffer changes that occur upon power application between incubation buffer and background electrolyte and have an influence on the reaction mixture.

Key words: capillary electrophoresis, enzyme reaction, electrophoretically mediated microanalysis, diffusion, simulation, Taylor-Aris dispersion

1. Introduction

During the last three decades, capillary electrophoresis (CE) became a powerful technique providing accurate and highly efficient analyses in many areas, including drug metabolism studies, requiring only minuscule amounts of sample and chemicals. The commonly used CE-based enzyme assay modes comprise two categories, namely (i) pre-capillary (off-line) assays in which the reaction mixture is incubated in a vial and the reaction products are analyzed by CE, and (ii) in-capillary (on-line) assays where incubation of a reaction mixture and analysis of reaction products are carried out in the capillary. Due to the small inner diameter of the capillary, the latter approach provides true nanoliter-scale assays and fulfills the demand of the pharmaceutical industry for miniaturized, fully automated screening systems [1,2]. An on-line method typically consists of four steps, consecutive injection of enzyme and reactant solution plugs and their mixing, incubation of reaction mixture, application of voltage and detection of reaction products. The lengths of the injected plugs are one to two orders of magnitude larger compared to the inner diameter of the capillary. In combination with liquid incompressibility, this makes perfect mixing of individually injected plugs difficult and thus represents a bottleneck of on-line CE methods for activity, kinetic and inhibition studies of enzymes. Incomplete mixing provides heterogeneous distribution of enzyme and reactants and thus regions of different effective reaction rates leading to inaccurate values of pharmacokinetic and enzymatic parameters. Assessment of reaction mixture distribution is thus a crucial part of on-line CE assay.

In practice, plug injection effected by application of differential pressure constitutes an inherent part of the mixing process and determines the initial distribution of enzyme and reactants inside the capillary. Several processes contribute to mass transfer during injection, including translational movement along the capillary, diffusion along the capillary, and diffusion across the capillary. Due to the friction close to the capillary inner wall, each injected plug possesses a characteristic parabolic profile which can be described by the Poiseuille equation (Fig. 1). With respect to mixing principles, assays can be divided into two groups. Firstly, mixing of enzyme and reactants can be obtained with electrophoretic merging, a process referred to as electrophoretically mediated microanalysis (EMMA) [3,4]. The other method is based on transverse diffusion of laminar flow profiles (TDLFP) proposed by the group of Krylov [5,6]. This approach relies on the application of a relatively high differential pressure for a short time

period which makes the plugs strongly parabolic. Each injected plug penetrates into the preceding zone thereby creating longitudinal interfaces (Fig. 1). Even large molecules, such as enzymes, are able to diffuse across the distance of capillary radius or diameter in tens of seconds such that a relatively homogeneous reaction mixture is quickly formed by transverse diffusion [5-9]. Mixing by transverse diffusion can be studied with the TDLFP model of Krylov in Excel [5-8]. Another approach, reported here for the first time, is the use of a dynamic electrophoretic simulator in the diffusion mode. Electrophoretic simulators provide component distributions within the capillary as function of time [10-16]. Two one-dimensional simulators, GENTRANS [12] and SPRESSO [14], feature a module that calculates zone and boundary dispersion caused by hydrodynamic flow and molecular diffusion using the Taylor-Aris equation [17,18]

$$D_{i(eff)} = D_i\,[1 + \beta P_e^2] \quad \text{with } P_e = Ud/D_i \qquad (1)$$

where $D_{i(eff)}$ is the effective diffusion coefficient, D_i is the diffusion coefficient of species i in absence of pressure driven flow (molecular diffusion), U is the average velocity of the pressure driven flow, d is the inner diameter of the capillary, and β is a constant representing the cross sectional shape of the capillary. For a circular capillary with diameter d, $\beta = 1/192$ [19,20].

In a previous study, Stahl et al. used a dynamic electrophoretic simulator to study plug-plug mixing phenomena in EMMA associated with local conductivity changes [21]. This work demonstrates the importance of employing a simulator which considers changes in the electric field in order to understand sample mixing in EMMA. Dynamic EMMA computer models which provide insight into electrophoretic mixing of reactants in a uniform electric field do not consider changes of buffer composition induced by the electric field [22-24]. The goal of the presented study was to characterize the mixing of the enzyme and the reactants in the two on-line configurations presented in Fig. 1 using dynamic computer simulation. These arrangements were previously employed for studying the enantioselective metabolism of ketamine mediated by the cytochrome P450 3A4 isoform (CYP3A4) enzyme. The four-plug configuration of Fig. 1A was used with voltage applied for a short time prior to incubation [25] and the seven-plug arrangement of Fig. 1B was employed in the TDLFP format [26]. Incubation occurred at physiological pH and analysis of formed norketamine enantiomers was achieved in a low pH background electrolyte (BGE) in presence of a negatively charged chiral selector. For both

systems, diffusional reactant mixing occurring during hydrodynamic plug insertion was analyzed with the GENTRANS simulator in the diffusion mode and compared to that predicted with the TDLFP model of Krylov. For the four-plug configuration, GENTRANS in the electrophoresis mode was employed to study the effect of power application on mixing after plug insertion, the use of alternative initial plug arrangements, and the impact of buffer changes occurring upon current flow at the discontinuity between incubation buffer (IB) and BGE. Experimental data were assessed on the basis of enantioselective norketamine analysis in the two on-line formats and compared to the predictions obtained by simulation. Furthermore, application of the cofactor reduced β-nicotinamide adenine dinucleotide phosphate (NADPH) as pure compound or with a regenerating system was also examined.

2. Materials and methods

2.1. Chemicals, reagents and solutions

Racemic ketamine and norketamine (as hydrochloride solutions in methanol, 1 mg/mL of the free base) were from Cerilliant (Round Rock, TX, USA). NADPH was purchased from Sigma-Aldrich (Buchs, Switzerland) as tetra sodium salt. Phosphoric acid (85%), potassium dihydrogen phosphate, and di-potassium phosphate were from Fluka (Buchs, Switzerland), and Tris from Merck (Darmstadt, Germany). Highly sulfated γ-cyclodextrin (HS-γ-CD) (20%) was purchased from Beckman Coulter (Fullerton, CA, USA). SUPERSOMES^{TM} containing human CYP3A4, P450 reductase and cytochrome b5 and the NADPH regenerating system (NADPH-RS) were obtained from BD Gentest (Woburn, MA, USA; distributed through Corning, Wiesbaden, Germany). The NADPH-RS comprises two solutions, solution A with $NADP^+$, glucose-6-phosphate and $MgCl_2$ and solution B with glucose-6-phophate dehydrogenase in sodium citrate. The enzyme solution was divided into aliquots and stored at -80 °C whereas NADPH-RS aliquots were kept at -20 °C. A stock solution of 10 mM NADPH was titrated to pH 8.0 with addition of 0.1 M NaOH and stored as aliquots at -20 °C. The pH 7.4 IB was prepared with 100 mM solutions of K_2HPO_4 and KH_2PO_4. The plug solutions were prepared daily in IB. The plug containing NADPH-RS was composed of solution A (25.00 %), solution B (5.00 %), IB (61.00 %), ketamine solution (7.15 %) and 1 M NaOH (1.85 %) [25].

2.2. Capillary electrophoresis

A ProteomeLab PA 800 CE System (Beckman Coulter, Fullerton, CA, USA) equipped with a photodiode array UV-VIS detector at 195 nm was used for all experiments and analyses were carried out as described before [25,26]. Briefly, the bare 50 µm id (375 µm od) fused-silica capillaries (Polymicro Technologies , Phoenix AZ, USA) were of 0.45 m total length (0.35 m effective length, [25]) and 0.60 m of total (0.50 m effective length, [26]). BGE was composed of 50 mM Tris-phosphate buffer (pH 2.5) and HS-γ-CD as a chiral selector (2 % v/v [25] and 3 % v/v [26]). The four-plug approach included a 3.5 min cooling period between the incubation (37°C) and separation (25°C) [25], whereas the seven-plug method was executed at 37°C [26]. Separations were performed by concomitant application of voltage (four-plug method: -12 kV, 266.7 V cm^{-1}, observed current about -41 µA; seven-plug method: -20 kV, 333.3 V cm^{-1}, about -86 µA) and positive pressure towards anode (0.1 psi (0.7 kPa) for both approaches). Data was acquired and peak areas were determined using the 32 Karat 7.0 software (Beckman Coulter). Results were reported as corrected peak areas, i.e. peak areas divided by migration time (units: µAU).

2.3. Conditions for in-capillary reaction

For the four-plug configuration of Fig. 1A and if not stated otherwise, each plug was injected by application of 1 psi (6.9 kPa) for 4 s, providing plug volumes of about 13.6 nL each. The overall length of the entire four-plug assembly was calculated to be approximately 27.6 mm (7.9 % of total capillary length). Furthermore, in selected experiments, application of -10 kV (222.2 V/cm) for 12 s (ramping for 10 s) was applied after insertion of the plugs. The configuration of Fig. 1B comprised an alternate injection of 4 plugs of ketamine and NADPH solution and 3 plugs of CYP3A4 solution. Each plug of the substrate and cofactor was injected for 3 s into the capillary at a pressure of 0.5 psi (3.45 kPa) and each plug of CYP3A4 SUPERSOMES was introduced by application of a negative pressure of -0.5 psi (-3.45 kPa) for 4 s. The use of negative pressure for CYP3A4 SUPERSOMES insertion provided better repeatability of the injection procedure [26]. The calculated plug volumes were approximately 3.8 and 5.1 nL, respectively. The estimated volume of the entire seven-plug assembly thus was 30.6 nL (15.5 mm or 3.1 % of total capillary). In both methods, the inlet capillary tip was washed by dipping in IB after each injection in order to minimize the mass transfer between the vials of the enzyme and reactants. Incubation time intervals at 37 °C used for the four- and seven-plug approaches were 8 and 10

169 min, respectively. The reference samples of norketamine production were prepared by off-line
170 incubation of CYP3A4, ketamine and NADPH at the same concentration as was estimated for
171 on-line assays. The reaction mixtures were incubated for a respective time period at 350 rpm and
172 37°C in a thermomixer (Eppendorf, Germany).

173 2.4. Tools for simulation, input data, data evaluation and execution of simulations

174 All computations were executed on Windows 7-based PCs with a 32bit operation system. The
175 reactants distribution in the capillary was investigated by GENTRANS using the version
176 comprising Taylor-Aris diffusivity which accounts for dispersion due to the parabolic flow
177 profile [12] and the TDLFP model of Krylov in Excel [6] which was downloaded from
178 www.chem.yorku.ca/profs/krylov. Electrophoretic mobilities of reactants in IB were determined
179 by CE using standard methods and short end injection according to Williams and Vigh [27].
180 Sample plug lengths and the velocity of the imposed applied flow were estimated with the CE
181 Expert Lite software (Beckman Coulter, Fullerton, CA, USA) and buffer compositions, ionic
182 strength and component mobilities were calculated using Peakmaster 5.2 software (downloaded
183 from http://www.natur.cuni.cz/Gas [28]). SigmaPlot 12.5 (Systat Software, San Jose, CA, USA)
184 was used for data presentation and statistical analysis of experimental data.

185 For the simulations with GENTRANS, NADPH was applied as cofactor and a protein with a pI
186 of 8.6 represented the CYP3A4 SUPERSOMES. If not stated otherwise, the plugs comprised IB
187 composed of 100 mM H_3PO_4 and 161 mM KOH with a calculated pH of 7.40 together with
188 either 400 nM of a protein (CYP3A4 SUPERSOMES) or 1 mM ketamine hydrochloride together
189 with 2 mM NADPH or no additional components. The BGE was composed of 77 mM H_3PO_4, 50
190 mM Tris, 7.6 mM of a negatively charged chiral selector and 7.6 mM sodium from the chiral
191 selector. The calculated pH of the BGE was 2.51. Physico-chemical input constants used are
192 summarized in Table 1. Initial zone structures with plugs of realistic lengths and sharp
193 boundaries were established and shifted along the 50 µm ID capillary for specified time intervals
194 with and without applying Taylor-Aris diffusivity. The capillary length was 10 cm and divided
195 into 10000 segments (Δx = 10 µm).

196 **3. Results and discussion**

3.1. Simulation of diffusional mixing during plug injection

GENTRANS was employed to estimate diffusional mixing of the enzyme and the reactants for the four-plug and seven-plug configurations of Fig. 1 using injection velocities of 1800 µm/s and 600 µm/s, respectively. Computer predicted concentration profiles for protein, ketamine and NADPH inside the capillary introduced by the four-plug injection procedures of Fig. 1A and the seven-plug method of Fig. 1B are shown in Fig. 2A and 2B, respectively. Profiles depicted are those for 16 s and 24 s, respectively, the time intervals used for insertion of the plugs in the two approaches. Distributions of the buffer components are not presented. Initial distributions of the protein and the reactants are depicted as inserts on the left hand side of each panel and the profiles predicted without Taylor-Aris diffusivity, i.e. with molecular or longitudinal diffusion only, for the respective time intervals are shown as inserts on the right side in each panel. These data indicate that mixing by transverse diffusion is effective whereas mixing by longitudinal diffusion can be neglected. This is in agreement with conclusions made by Krylova et al. [8].

The data presented in Fig. 2A reveal that introduction of one plug of protein solution and one plug of ketamine and NADPH solution results in partially overlapping zones. It is also apparent that the protein becomes stronger dispersed compared to the low molecular mass components. The same behavior is true with injection of narrower zones. In the case of the seven-plug configuration of Fig. 1B, simulation with GENTRANS predicts a good distribution of the protein throughout the zone structure (Fig. 2B). In contrast, low-molecular-mass reactants become again less dispersed. This difference is due to the much lower diffusion coefficient of a protein (Table 1). The lower diffusion coefficient results in a larger Taylor-Aris diffusivity (cf. Eq. 1) and thus enhanced transverse diffusion for the protein. The diffusion value used (Table 1) is typical for a protein [10]. No value was available for CYP3A4 SUPERSOMES. CYP3A4 in the purchased SUPERSOMES is membrane bound and probably has a lower diffusion coefficient than albumin. Based on efforts dealing with CYP2C9 SUPERSOMES, a diffusion coefficient of 1.34 $\times 10^{-11}$ m^2/s was reported for that system [29]. Using this value instead of 5.94 $\times 10^{-11}$ m^2/s resulted in an even broader Aris-Taylor dispersion (red broken line graph in Fig. 2A). For the investigations made in our work, an exact value is not required as spreading of the protein is sufficient for both cases. The diffusion coefficient of NADPH used (64.21 $\times 10^{-11}$ m^2/s) corresponds to the value given in [29] and was also employed for ketamine. These values may

not be accurate but they provide sufficient insight into the principle of mixing by transverse diffusion when plugs are inserted with a specified velocity. It is important to note that, for small molecular mass components, GENTRANS requires the input of a mobility value and calculates the diffusion coefficient via the Einstein relation (Table 1).

The data presented in Fig. 2 suggest that transverse diffusion provides mixing of the reactants in both configurations. Similar results were obtained with the Krylov model (Fig. 3A and 3B), a model which considers differences in the total hydrodynamic transport time intervals of the plugs (time intervals decrease from firstly to lastly injected plug), neglects longitudinal molecular diffusion, and provides profiles of enzyme and reactants only. GENTRANS considers both transverse and longitudinal dispersion, handles reactant and buffer components, and thus provides also distributions of buffer constituents (Fig. 4A), pH (Fig. 2, 4A) and conductivity (Fig. 4C). Thus, intrusion of BGE components into the reaction zone is not handled by the Krylov model but is visualized by GENTRANS. In the case of the four-plug configuration with the firstly introduced plug composed of IB only, penetration of the chiral selector into the reaction zone and thus complexation of ketamine which affects the enzymatic reaction is prevented. Furthermore the pH of 7.40 is maintained throughout the reaction mixture (Fig. 2A). For the seven-plug structure, a small part of the reaction mixture is predicted to be affected by the BGE (right hand side of mixture in Fig. 2B). This could easily be prevented by commencing the plug injection procedure with a plug of IB as was the case for the four-plug configuration (Fig. 1A).

3.2. Simulation of electrophoretic mixing and buffer changes after plug injection

In the previous work with the four-plug structure and employing the NADPH regenerating system to promote the enzymatic reaction, short application of voltage (-10 kV for 10 s) just after hydrodynamic plug injection followed by the incubation period without applied electric field revealed enhanced norketamine formation [25]. Thus, simulation with GENTRANS was employed to provide insight into the processes occurring during this period. For the four-plug system of Fig. 2A, distributions of enzyme, reactants, buffer components and pH after plug injection are shown in Fig. 4A. The impact of application of a constant -1000 V (100 V/cm) for 16 s without buffer flow is presented in Fig. 4B. Under the influence of the electric field, ketamine is predicted to migrate towards the cathode (left hand side in Fig. 4B) and NADPH

towards the anode (right hand side). In the same time interval, the distribution of CYP3A4 is predicted to remain almost the same (very small displacement towards the cathode). Application of power is predicted to provide a better mixing of ketamine with the enzyme (in an EMMA type fashion). However, NADPH is migrating in the opposite direction and responsible for a smaller overlap with the other reagents. Thus, the application of power should result in a somewhat smaller reaction mixture of the three components and should not enhance metabolite production. This is in agreement with experimental data obtained with this configuration (Fig. 5B, case I). A typical electropherogram which was obtained with the application of the short power pulse prior to incubation is presented in Fig. 5A. As expected the yield of S-norketamine was larger than that of R-norketamine. This is in agreement with the data reported before [25]. The voltages applied in the experiment and simulation (222.2 V/cm with 0.17 min ramping and 100.0 V/cm with no ramping, respectively) were similar but not equal. Thus, in order to obtain comparable results, a 16 s time interval of voltage application was used in the simulation rather than the 12 s of the experiment.

Simulations with GENTRANS provide information about the dispersion and migration of all components, including the buffer constituents (Fig. 4). This is of particular interest in the context of the two buffers used (IB and BGE) which have a different composition and a completely different pH (7.40 vs. 2.51, respectively) and conductivity (2.04 vs. 0.49 S/m, respectively, Fig. 4C). The IB provides the right environment for the enzymatic reaction whereas the BGE serves as medium for the enantioselective separation and analysis of the formed metabolites. The buffer change, after hydrodynamic displacement, is located at 5.6 cm of the simulation column (Fig. 4A). Upon voltage application, the negatively charged chiral selector becomes removed from the anodic edge of the incubation mixture and a number of concentration boundaries begin to develop. To simplify matters, the chiral selector was modeled as a monovalent strong acid (Table 1). Two sharp steady-state moving boundaries that migrate towards the cathode and define the beginning and end of a sodium buffer zone were formed on the anodic side of the potassium based IB (Fig. 4B). These boundaries are formed because the effective electrophoretic mobility of potassium is larger than that of sodium and the mobility of sodium is larger than that of Tris. Sodium originates from the chiral selector in the BGE, migrates towards the cathode and its zone becomes longer with time. Due to Tris in the BGE, a new buffer which contains sodium, Tris and phosphoric acid is formed on the anodic side of the sodium zone. The pH of this buffer is

predicted to be 7.22 and is slightly lower compared to that of the IB (7.40) whereas the conductivity is significantly smaller (0.77 vs. 2.04 S/m, Fig. 4C). Furthermore, two boundaries migrate towards the anode (Fig. 4B) with one migrating very slowly and representing a large pH change. A stationary boundary is formed at the location of the initial buffer change (from IB to BGE, visualized with the buffer distributions depicted in Fig. 4A). These data suggest that with prolonged application of voltage (e.g. > 40 s) incubation would occur in the sodium-Tris-phosphate buffer and not in the foreseen IB.

For the data presented in Figs. 2-4, the input data summarized in Table 1 were used. For the enzyme and the two reactants, these data are not accurate but reflect the principle. The effective electrophoretic mobility of the weak base ketamine in IB (pH 7.4, ionic strength of 222 mM) was determined to be 1.00×10^{-8} m^2/Vs. The pKa value of ketamine is 7.5 (Table 1) which indicates that ketamine in IB is about 50 % protonated. Using Peakmaster and considering the ionic strength, the limiting ionic mobility of ketamine was estimated as 2.35×10^{-8} m^2/Vs. This mobility is close to the 2.50×10^{-8} m^2/Vs used in the simulation (Table 1). The effective mobility of NADPH in IB was found to be 2.98×10^{-8} m^2/Vs and NADPH migrated as an anion. NADPH is a multivalent component and supplied as tetra sodium salt. No exact pKa values were available. Thus, in order to mimic the anionic transport in the electric field, NADPH was treated as a monovalent weak acid with a pKa value of 2.0 and a mobility of 2.50×10^{-8} m^2/Vs (Table 1). The migration behavior of CYP3A4 SUPERSOMES could not be studied experimentally as the concentration in the purchased reagent was too small. CYP3A4 is claimed by the SUPERSOMES distributor to have a pI value around 8.6 (Dr. M. Gueldenagel, Scientific Support, Corning, email message of November 25, 2014). Thus, the input titration curve for the protein was created around this pI value [10]. With this input, the protein is slightly positively charged at pH 7.40. It is not known how realistic this input is as SUPERSOMES comprise also the electron donor partners P450 reductase and cytochrome b5 which are negatively charged proteins at pH 7.4. In SUPERSOMES, all three proteins are membrane bound and there is no information available about the stability of the vesicle in the electric field [30]. These facts, however, are not terribly disturbing as the low diffusion coefficient results in sufficient overlap of the SUPERSOMES with the two reagents during the hydrodynamic injection.

Experimental results obtained with NADPH-RS as originally used in [25] instead of NADPH are presented as case Ia in Fig. 5B. The norketamine production yields obtained for this configuration are equal to those observed with NADPH (case I of Fig. 5B). Both approaches provide lower norketamine amounts compared to off-line incubation (case off-line of Fig. 5B). With the use of NADPH-RS, however, application of voltage resulted in an increased production of norketamine enantiomers. This is in agreement with previous data [25] and is different compared to case I of Fig. 5B. Reasons for the enhancement of metabolite production upon voltage application are not clear. The NADPH-RS reagent mixture comprises $NADP^+$, glucose-6-phosphate, $MgCl_2$, glucose-6-phosphate dehydrogenase and sodium citrate. Due to lack of proper input data for most of these compounds, the dynamics of such a configuration under current flow could not be simulated.

3.3. Analysis of alternative four-plug arrangements

In order to further validate the simulation approach used to study diffusional and electrophoretic mixing in Sections 3.1. and 3.2., respectively, three alternative four-plug arrangements were investigated. These configurations comprised ketamine in the plug with CYP3A4 SUPERSOMES instead of the plug with NADPH (referred to as case II), NADPH in the SUPERSOMES plug instead of the plug with ketamine (case III) and NADPH injected after CYP3A4 SUPERSOMES (case IV). They were studied by computer simulation using GENTRANS and examined experimentally both without and with application of voltage for a short time after hydrodynamic injection of the plugs. Based on simulations, configuration II should not provide an improvement compared to the case shown in Fig. 4. With application of the electric field, ketamine and NADPH are predicted to migrate in opposite directions such that there is less overlap of these reactants and metabolite production became diminished as was found for case I (data not shown). Data obtained with NADPH in the enzyme plug are presented in Fig. 6A. Electrokinetic mixing is predicted to provide a larger overlap of the three reactants as NADPH and ketamine are migrating towards each other (compare solid line graphs with broken line graphs of Fig. 6A). Simulation conditions used were the same as those for Fig. 4 such that the data can be directly compared. Thus, for case III, application of voltage should result in an increased metabolite production. The performed experiments confirmed this prediction (insert Fig. 6A). This configuration, however, is not suitable from a practical point of view as NADPH

347 and CYP3A4 SUPERSOMES should not be combined because of gradual NADPH degradation
348 caused by CYP reductase.

349 Data obtained for case IV are presented in Figs. 6B and 6C. This configuration should provide
350 the best injection order of reactants for an EMMA based analysis. The first injected plug with IB
351 keeps the BGE separated from the incubation mixture, the second plug poses the substrate
352 ketamine with its positive electrophoretic mobility, the third plug provides CYP3A4
353 SUPERSOMES and the last plug applies NADPH with its negative electrophoretic mobility.
354 Introduction of the plugs is predicted to provide no overlap of NADPH and ketamine (broken
355 line graphs in Fig. 6B) whereas reactant mixing is obtained via electrophoretic transport (solid
356 line graphs in Figs. 6B and 6C). This was experimentally confirmed with no norketamine
357 enantiomers being detected without whereas norketamine enantiomers were monitored after
358 electrokinetic mixing (insert Fig. 6B). The time interval used to study the effect of
359 electrophoretic mixing was twice as long compared to that used for the other configurations.
360 During electrophoretic mixing, buffer changes occur as was discussed above for Fig. 4B. The
361 cationic moving boundary system produced upon current flow behind the leading potassium ion
362 is predicted to migrate faster towards the cathode than ketamine. It thus overtakes ketamine
363 which becomes adjusted to a narrower peak with higher concentration (about 2.08 mM, Fig. 6C).
364 The asterisks in panel B of Fig. 6 mark the locations of the two moving boundaries after 32 s of
365 power application. NADPH on the other hand is predicted to become a broader peak with a
366 concentration maximum around 1.32 mM (Fig. 6C). Part of this process for ketamine is seen in
367 the 32 s distribution presented as solid line graph in Fig. 6B. Complete overlap of both reagents
368 is predicted to occur after 64 s of power application (Fig. 6C). During this merging process at a
369 constant -1.0 kV the current density dropped from -9499.6 A/m^2 to -8564.7 and -7895.2 A/m^2
370 after 32 s and 64 s of power application, respectively. Only one moving boundary migrating
371 towards the cathode would be obtained with the use of sodium instead of potassium in the IB and
372 no cationic migrating boundary (i.e. no buffer change) is predicted with sodium in the IB and no
373 Tris in the BGE (e.g. with 50.14 mM NaOH instead of 50 mM Tris in BGE). Thus, with the
374 latter buffer system, the profiles of the reactants would not deteriorate as is seen in the data of
375 Fig. 6C. These data reveal that simulation provides meaningful data in all four cases.

376 3.4. Experimental results with the seven-plug arrangement

Norketamine production data obtained with the seven-plug approach are presented in Fig. 7. The first configuration assessed was that adopted from the literature [26] for which a typical electropherogram is depicted in Fig. 7A. Data of determined peak areas are presented as case I in Fig. 7B. As expected the yield of S-norketamine was larger than that of R-norketamine. This is in agreement with the data reported before [26]. Furthermore, a 2.5-fold reduction of the plug insertion velocity (0.2 psi instead of 0.5 psi) together with 2.5-fold higher injection times such that the same plug volumes were injected resulted in a much smaller production of the norketamine enantiomers (case I (0.2 psi) of Fig. 7B). These data nicely illustrate that transverse diffusional mixing is dependent on the injection velocity of the plugs as is predicted by Eq. 1 and also confirms the predictions of the TDLFP model.

The use of NADPH-RS instead of NADPH in the ketamine solution (case Ia of Fig. 7B) provided a somewhat higher norketamine production yield compared to that with NADPH (case I of Fig. 7B). Similar data were obtained with off-line incubation (case off-line of Fig. 7B). These data reveal that plug injections at 0.5 psi (injection velocity of about 600 µm/s) provide good conditions for transverse diffusional reactant mixing in the seven-plug approach. The employment of NADPH-RS demonstrated no significant advantage over simple addition of NADPH in terms of norketamine production.

4. Concluding remarks

The data presented reveal that dynamic computer simulation provides meaningful data for transverse diffusional reactant mixing occurring during plug injection and electrophoretic reactant mixing caused by voltage application after plug insertion. Furthermore, reactant adaptation due to buffer changes which occur upon current flow when a discontinuous buffer system is employed can be investigated and visualized with the same simulator. From the results obtained it is obvious that the injection velocities used experimentally were effective to provide sufficient transverse diffusional reactant mixing during hydrodynamic plug insertion in both plug configurations. Due to the longer plugs employed in the four-plug arrangement, a higher plug injection velocity was required to reach sufficient diffusional mixing. Compared to the seven-plug system, the four-plug configuration provides a less defined reaction space. In the latter approach, partial overlap of enzyme and reactants is obtained only. In all cases analyzed, the

predicted mixing of reactants and enzyme could be validated experimentally for the enantioselective N-demethylation of ketamine to norketamine mediated through CYP3A4. No fundamental difference between the use of NADPH and NADPH-RS was found. Both cofactor sources supply enough reducing equivalents for the enzymatic reaction. The simulation efforts conducted in this work illustrate the value of using a dynamic simulator to investigate both diffusive and electromigrational aspects of mass transport in on-line systems.

Conflict of interests

The authors have declared no conflict of interests.

Acknowledgements

This work was supported by the Swiss National Science Foundation.

References

[1] J.J. Bao, J.M. Fujima, N.D. Danielson, Determination of minute enzymatic activities by means of capillary electrophoretic techniques, J. Chromatogr. B 699 (1997) 481–497.

[2] Z. Glatz, Determination of enzymatic activity by capillary electrophoresis, J. Chromatogr. B 841 (2006) 23–37.

[3] J.J. Bao, F.E. Regnier, Ultramicro enzyme assays in a capillary electrophoretic system, J. Chromatogr. 608 (1992) 217–224.

[4] S. Van Dyck, J. Hoogmartens, A. Van Schepdael, Michaelis-Menten analysis of bovine plasma amine oxidase by capillary electrophoresis using electrophoretically mediated microanalysis in a partially filled capillary, Electrophoresis 22 (2001) 1436–1442.

[5] V. Okhonin, X. Liu, S.N. Krylov, Transverse diffusion of laminar flow profiles to produce capillary nanoreactors, Anal. Chem. 77 (2005) 5925–5929.

[6] S.M. Krylova, V. Okhonin, S.N. Krylov, Transverse diffusion of laminar flow profiles – a generic method for mixing reactants in capillary microreactor, J. Sep. Sci. 32 (2009) 742–756.

[7] E. Wong, V. Okhonin, M.V. Berezovski, T. Nozaki, H. Waldmann, K. Alexandrov, S.N. Krylov, "Inject-Mix-React-Separate-and-Quantitate" (IMReSQ) method for screening enzyme inhibitors, J. Am. Chem. Soc. 130 (2008) 11862–11863.

[8] S.M. Krylova, V. Okhonin, C.J. Evenhuis, S.N. Krylov, The Inject-Mix-React-Separate-and-Quantitate (IMReSQ) approach to studying reactions in capillaries, Trends Anal. Chem. 28 (2009) 987–1010.

[9] R. Řemínek, M. Zeisbergerová, M. Langmajerová, Z. Glatz, New capillary electrophoretic method for on-line screenings of drug metabolism mediated by cytochrome P450 enzymes, Electrophoresis 34 (2013) 2705–2711.

[10] R.A. Mosher, D. Dewey, W. Thormann, D.A. Saville, M. Bier, Computer simulation and experimental validation of the electrophoretic behavior of proteins, Anal. Chem. 61 (1989) 362–366.